In-Vitro Investigation on the Tribological Properties of Nickel-Titanium (NiTi) Alloy Used in Braided Vascular Stents

Yeping Peng, Deyu Kong, Song Wang, Guang-Zhong Cao & Chaozong Liu

Yeping Peng[a], Deyu Kong[a], Song Wang[b], Guang-Zhong Cao[a], and Chaozong Liu[c]

[a]Guangdong Key Laboratory of Electromagnetic Control and Intelligent Robots, College of Mechatronics and Control Engineering, Shenzhen University, Shenzhen, P. R. China; [b]University in Shenzhen, Biomechanics and Biotechnology Laboratory, Research Institute of Tsinghua, Shenzhen, P. R. China; [c]Institute of Orthopaedics and Musculoskeletal Science, University College London, Royal National Orthopaedic Hospital, London, UK

ABSTRACT

The integration of diverse weaving angles in vascular stent design proves beneficial for addressing complex applications such as bending, branching, and load-bearing. However, the weaving pro- cess may introduce frictional corrosion issues among threads, necessitating further investigation into frictional behaviors at different weaving angles. This study simplifies the contact between nickel-titanium (NiTi) alloy threads in woven stents as line-to-line contact between rods. A pro- posed in vitro experiment, based on weaving angles of 30°, 45°, 60°, 75°, and 90°, systematically analyzes friction and wear characteristics, including friction coefficients, wear parameters, and morphology. Findings indicate significant impacts of weaving angles on tribological behaviors, with 30° weaving angle stents exhibiting the lowest wear rate. The study identifies four develop- mental stages in the life cycle of line-to-line contact wear: breaking-in wear, steady wear, severe wear, and post-stable wear. Under 25% calf serum lubrication, lower friction coefficients and wear rates are observed, validating NiTi alloy suitability for lubricated human environments. The investi- gation reveals a nonlinear correlation between weaving angles, friction cycles, and wear rates, offering insights for the tribological design of woven instruments.

Introduction

The interventional procedure involving vascular stents has become a prevalent and effective treatment modality for vas- cular ailments. (1) While most current stents are produced using laser engraving technology, they exhibit weaknesses in supporting force, susceptibility to folding, and poor fatigue fracture performance, potentially leading to catastrophic complications. To address these issues, braided vascular stents woven from NiTi alloy wire have been developed, offering flexible braiding characteristics suitable for applica- tion in complex environments such as curved, bifurcated, and moving limbs blood vessels.

However, the inevitable occurrence of frictional wear among the filaments of braided stents, (2,3) combined with mechanical stresses from prolonged exposure to blood flow dynamics and vascular compression, (4) triggers wear, fatigue, and the eventual failure of vascular stents. Moreover, the subsequent production of wear debris may lead to stent restenosis and vessel occlusion recurrence. (5) Enhancing wear resistance and biocompatibility becomes crucial for ensuring the therapeutic efficacy of vascular stents.

Extensive documentation exists on simulation experi- ments examining the wear performance of overlapping braided stents. (6) These investigations primarily focus on three crucial domains: the inherent wear characteristics of stent materials, (7,8) the effects of force patterns, (9) and shear stress (10–13) on wear dynamics, as well as the opti- mization of stent design, including strategic coating approaches. (14–21)

Braided stents, particularly those crafted from single fila- ments, demonstrate commendable mechanical attributes. Advocates suggest a reduction in the braiding angle to miti- gate friction between stent layers. (2) Fatigue assessments on vascular stents through overlapping axial fatigue tests reveal frictional wear observed through optical microscopy and scanning electron microscopy. These investigations validate analogous wear patterns in two distinct materials: NiTi alloy and stainless steel. (22) In particular, the tribological proper- ties of scaffolding assembly are significantly impacted by the sliding wear mode between cylindrical components. (23,24) Investigation on wear behaviors of

scaffolding assembly merits can provide a reference for performance evaluation and optimal design.

In the pursuit of enhancing the wear properties of vascu-lar stents, the incorporation of a titanium nitrogen (TiN) coating onto NiTi alloy has been explored. Tribological experimentation confirms its nanomechanical, tribological, and cytotoxic attributes. (25) Nevertheless, the level of wear susceptibility depends on various factors, including friction angle, lubricant, and loading force. (8) Thus, a comprehen- sive multifactorial analysis regarding stent wear assumes utmost importance.

The widespread use of NiTi alloy in vascular stents is attributed to its exceptional biocompatibility. (26) However, initial trial testing outcomes have revealed instances of fail- ures linked to the wear process within braided stents and ensuing biological reactions caused by wear debris. (27,28) To unveil the bio-tribological properties intrinsic to NiTi alloy as a vascular stent material, this paper introduces a comprehensive research methodology designed to evaluate the frictional wear performance of NiTi alloy.

The friction pairs are meticulously structured to include diverse angles, subsequently exposed to experimental condi- tions involving varied loads and lubricants, simulating intri- cate in-vivo environments. Simultaneously, the gathering of data on friction coefficients and worn surface morphologies under diverse working conditions forms the basis for assess- ing wear degree, wear mechanisms, and bio-performance characteristics. The contributions of this work are as follows:

1. The long-term wear behavior inherent to NiTi friction pairs is analyzed to provide reference for improving the friction and wear performance of braided vascular stent.

2. The impacts of friction angle on the wear performance of vascular stent interfaces are investigated, which is helpful determine the braid angle of braided vascular stents.

Comparative analysis of dry friction, phosphate-buffered saline (PBS), and 25% calf serum lubricated friction regimes is conducted for comprehensive analysis of the tribological properties in vitro investigation.

Materials and methods

Experiment materials

For the emulation of tribological behaviors inherent to NiTi vascular stents, the friction pairs—consisting of both upper and lower components—are crafted from biomedical NiTi alloy material. Typically, the diameter of vascular stent filaments spans from 0.1 to 0.2 mm. To alleviate the complexities associated with filament clamping, the NiTi alloy was fashioned into a solid bar material, exhibiting a diameter of 5 mm and a length of 20 mm. By doing so, the wear progress is accelerated to obtain different wear status of the friction pairs.

Aiming to mitigate any potential interference stemming from varying surface roughness, a polishing process was undertaken, culminating in a surface roughness measuring below 2 1m. The elemental composition of the utilized NiTi alloy adheres to prevailing medical standards.

Design of experiments

To examine the impact of distinct angular displacements between the interwoven layers of the vascular stent on both

wear rate and wear mechanisms, the friction angles were designated as $30^{\natural}$, $45^{\natural}$, $60^{\natural}$, $75^{\natural}$, and $90^{\natural}$. As a consequence of the variable forces exerted by blood flow and vascular compression, the forces applied to the frictional interfaces exhibited notable disparities.

To accurately emulate the intricate friction and wear dynamics characteristic of vascular stents, the experimental design meticulously encompassed three pivotal working conditions: diverse friction angles, varying lubrication scenarios, and a precise quantification of friction cycles. Aligned with insights derived from a precedent scholarly inquiry, ([6]) the motion frequency of the friction pairs was specified at 2 Hz, coupled with a precisely calibrated acceleration of 0.1 m/s². Noteworthy was the numerical delineation of the experimental endeavor, reflected in the choice of 2,400, 7,200, 14,400, 21,600, and 28,800 friction cycles. These values are employed to discern and evaluate the sequential evolution of wear stages across the designated intervals.

The investigation into lubrication conditions for NiTi wear testing predominantly centered on dry friction, physiological saline, and PBS buffer solutions. ([29–31]) Following the specifications delineated within ASTM F2477, ASTM F2942, and ISO 25539-1, the application of PBS or equivalent materials is widely recommended for durability assessments. ([14]) However, it is important to note that while PBS serves as a suitable benchmark for such purposes, its representation of the human blood environment is not exact. Consequently, alternative lubrication conditions, encompassing dry friction and calf serum, have been proposed. ([14]) Calf serum, containing a composition of proteins, hormones, and other constituents similar to those found in human blood, presents a more congruous emulation of physiological conditions. ([32,33]) To better replicate the human blood environment, a 25% volume fraction of calf serum, when diluted with PBS, was adopted as the chosen lubricating medium. The PBS not only has a buffer function, but also can maintain osmotic fluid balance, close to the internal environment. This approach seeks to provide a more realistic approximation of the conditions encountered within the human circulatory system.

Insight garnered from finite element simulations unveiled an approximate contact pressure of 4 N upon the vascular stent. ([6]) Consequently, within this study, loads were specifically stipulated as 30 N, in consideration of the NiTi alloy diameter, 5 mm. A series of eleven comparative experiments were undertaken to scrutinize the effects stemming from the aforementioned four distinct operational circumstances on the tribological attributes of the NiTi alloy, as outlined in Table 1.

In Table 1, all comparative experiments were executed under uniform conditions of 2 Hz frequency and 0.1 m/s² acceleration. In particular, the ramifications arising from variations in the number of friction cycles and friction angle, were investigated within the context of dry friction conditions. Concurrently, in alignment with the aforementioned three parameters, the consequences of dissimilar lubrication conditions, encompassing dry friction, PBS, and calf serum, were assessed.

Table 1. The design of comparative experiments.

Group number	Lubrication	Friction cycles	Friction angle (°)
Group 1	Dry friction	2,400	90
Group 2	Dry friction	7,200	90
Group 3	Dry friction	14,400	90
Group 4	Dry friction	21,600	90
Group 5	Dry friction	28,800	90
Group 6	Dry friction	14,400	30
Group 7	Dry friction	14,400	45
Group 8	Dry friction	14,400	60
Group 9	Dry friction	14,400	75
Group 10	PBS	14,400	90
Group 11	25% Calf serum	14,400	90
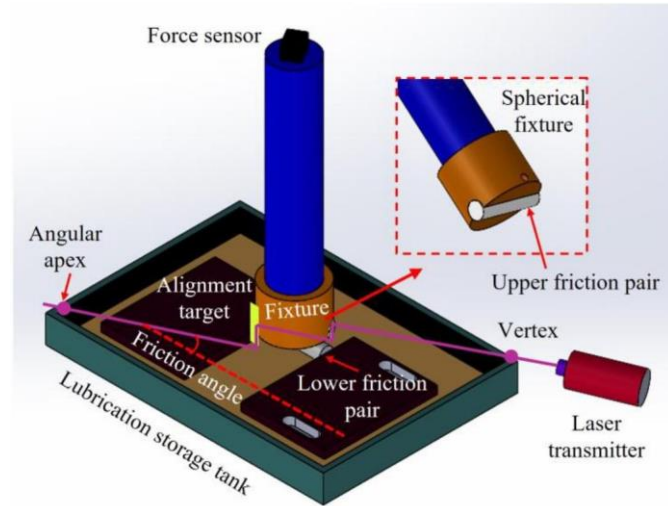
Figure 1. The schematic diagram of friction pair clamping apparatus.

Experiment methods

Tribology experiments

The reciprocating friction assessments of the NiTi material were conducted using a friction and wear testing apparatus. The clamping configuration for the frictional pair is depicted in Fig. 1. The lower element of the friction pair was positioned within a square recess designed to accommodate lubrication. Meanwhile, the upper counterpart of the friction pair was immobilized using a dedicated fixture. This fixture comprised a hollow cylindrical pin housing a threaded spherical clip, which was employed to firmly secure the NiTi alloy bar in place. Atop the cylindrical pin, a three-dimensional force sensor was situated to capture both the normal load force and the tangential frictional force, thereby enabling the precise determination of the friction coefficient.

In accordance with the data presented in Table 1, the measurements of the lubrication storage tank, configured in a square shape, were meticulously assessed to determine the angular juncture. During the loading procedure, a laser alignment system was utilized to ensure the precise alignment of the upper NiTi alloy bar with both the vertex and the angular apex of the square indentation. The alignment target was employed to aid in establishing the parallelism between the laser and the rod. This alignment was conducted with utmost precision to achieve the intended friction angle.

Extraction of tribological parameters

The friction coefficient during the wear progress was measured by the sensor of the friction and wear testing apparatus. Meanwhile, alterations in the wear amount of the frictional pairs were gauged through pre- and post-wear processes utilizing an electronic balance. The topographies of the worn surfaces underwent comprehensive analysis using both a scanning electron microscope (SEM) (34–36) and a laser scanning confocal microscope (LSCM). (37–39) To facilitate an in-depth scrutiny of wear behaviors, the roughness parameters of the worn surfaces were meticulously extracted in accordance with the ISO 25178 standard. The arithmetic mean height (Sa), maximum height (Sz), root-mean-square height (Sq), skewness (Ssk), and kurtosis (Sku) are used to evaluate the surface roughness.

Furthermore, an additional set of five parameters encompassing center section height (Sk), prominent peak height (Spk), prominent valley height (Svk), the load area ratio at the intersection of the upper center section height and the load curve ($Smr1$) and the load area ratio at the intersection of the lower center section height and the load curve ($Smr2$), were methodically derived. These parameters collectively contribute to the formulation of the Abbott-Firestone curve, (40,41) a tool employed for the quantitative assessment of the "peaks" and "valleys" on the surface.

Results

Tribological behavior analysis under different friction angles

Friction coefficient and wear rate

A comprehensive series of experiments were conducted, encompassing varied friction angles, 30°, 45°, 60°, 75°, and 90°, with the aims of assessing their impacts on tribological behaviors. The resulting curves illustrating the coefficient of friction (COF) are delineated in Fig. 2a. It is observable that the friction coefficients exhibit stability at different angles. Specifically, at friction angles of 30°, 45°, and 60°, the mean friction coefficients are 0.61757, 0.63971, and 0.6446, respectively, signifying an ascending trend. However, the pace of increase in the friction coefficient is attenuated. Beyond encompasses a friction angle of 60°, the friction coefficient tends to stabilize. Notably, at angles of 60°, 75°, and 90°, the severities of wear demonstrate similarity. Consequently, it is apparent that at smaller angles, there is a noteworthy mitigation of wear severity, yet this ameliorative effect diminishes as the angles increase.

Given the influence of friction angle on the contact area during the wear process, we conduct a comprehensive analysis of the relationship between wear amount and cross-sectional area. The variations in wear amount, wear cross-sectional area, and wear rate under different friction angles are illustrated in Fig. 2b–d. Owing to the change of wear area between cylindrical friction pairs, wear volume per unit time is not suitable for expressing the wear rate. Hence, wear volume per unit area is used as the indicator of wear rate to evaluate the wear severity, as shown in Fig. 2d.
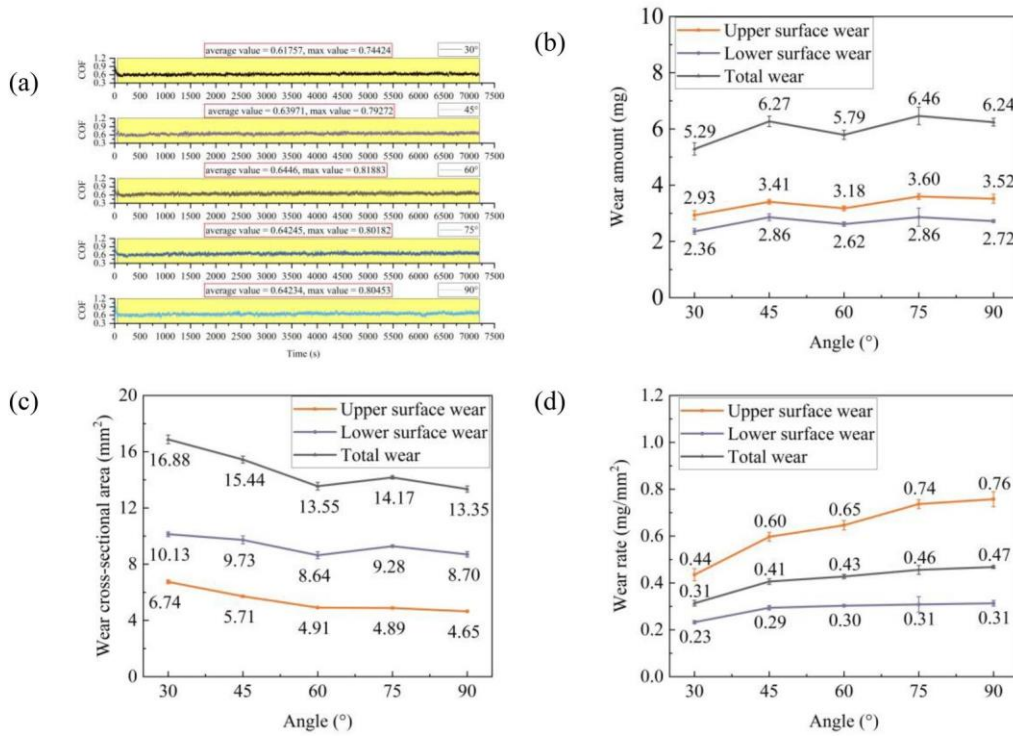
Figure 2. The wear results under different friction angles: (a) Coefficient of friction (COF) curve; (b) wear amount; (c) wear cross-sectional area; (d) wear rate.

The variations in wear amount, wear cross-sectional area, and wear rate under different friction angles are illustrated in Fig. 2b–d. It can be seen from Fig. 2b that the changes in wear amount exhibit an alternating trend with the increase in friction angles but overall show an upward tendency. The difference in wear amount between the upper and lower surfaces is approximately 0.6 mg. The total wear amount is at its lowest, 5.29 mg, at a friction angle of 30°, indicating that wear is minimum at lower angles.

From Fig. 2c, it can be observed that the wear cross-sectional area decreases at a constant rate when the friction angle is less than 60°. However, the wear cross-sectional area of the lower surface shows an upward trend followed by a downward trend when the friction angle exceeds 60°. A slight increase in total wear amount is shown at 75°, while the upper surface decreases at a smaller constant rate.

As depicted in Fig. 2d, the variation in wear rate indicates an upward trend with increasing angles. The wear rate increases most rapidly between 30° and 45°, and beyond 45°, and the rate of change in wear rate diminishes. Overall, wear exhibits a gradually decreasing upward trend with increasing friction angles, with the wear rate being lowest at 30°, indicating the least severe wear.

Furthermore, it is discernible that the material loss experienced by the upper friction pair surpasses that of the lower friction pair. This discrepancy arises from the dynamics of contact during reciprocating motion—wherein the upper friction surface remains stationary while the lower counterpart is in motion. This may result in a diminished contact area on the upper surface. Consequently, this configuration imparts heighten wear to the upper surface due to the localized contact dynamics.

Wear surface

Figure 3 is the SEM and LSCM images of the worn surfaces produced at different friction angles. It is observed from Fig. 3a–e that there is a significant variation between the wear areas with the increase of friction angle. At an angle of 30°, the wear rate is relatively mild, characterized by micro-scratches, micro-pits, and slight furrow morphology. The larger area exhibits a micro-rough surface with no deep wear features, primarily indicating adhesive wear. At friction angles of 45°, 60°, 75°, and 90°, the wear surfaces are mainly composed of significant scratches, accompanied by severe adhesive wear, leaving behind adhesive traces and adhesive peaks. Material accumulation occurs at both ends of the adhesive scratches, presenting a delamination structure. The worn surface edges show a tendency to fracture, making it prone to detachment and forming wear debris, leading to three-body wear. In addition, the worn surfaces are also embedded wear debris that are pressed and embedded by friction. Hence, adhesive wear and abrasive wear are the predominant types of wear mechanisms.

Figure 3f–j presents the lower worn surfaces generated at different angles. It is observed that there is a significant difference in the cross-sectional areas of the worn surfaces, while the surface wear morphologies are similar. The surfaces are mainly composed of peaks formed by material accumulation and adhesive traces left after adhesive wear. Sharp protruding edges may be present around the adhesive traces. Additionally, some abrasive debris remains or is embedded in the surface, creating numerous high-level structures. Significant adhesive traces are observed when the friction angle exceeds 30°.
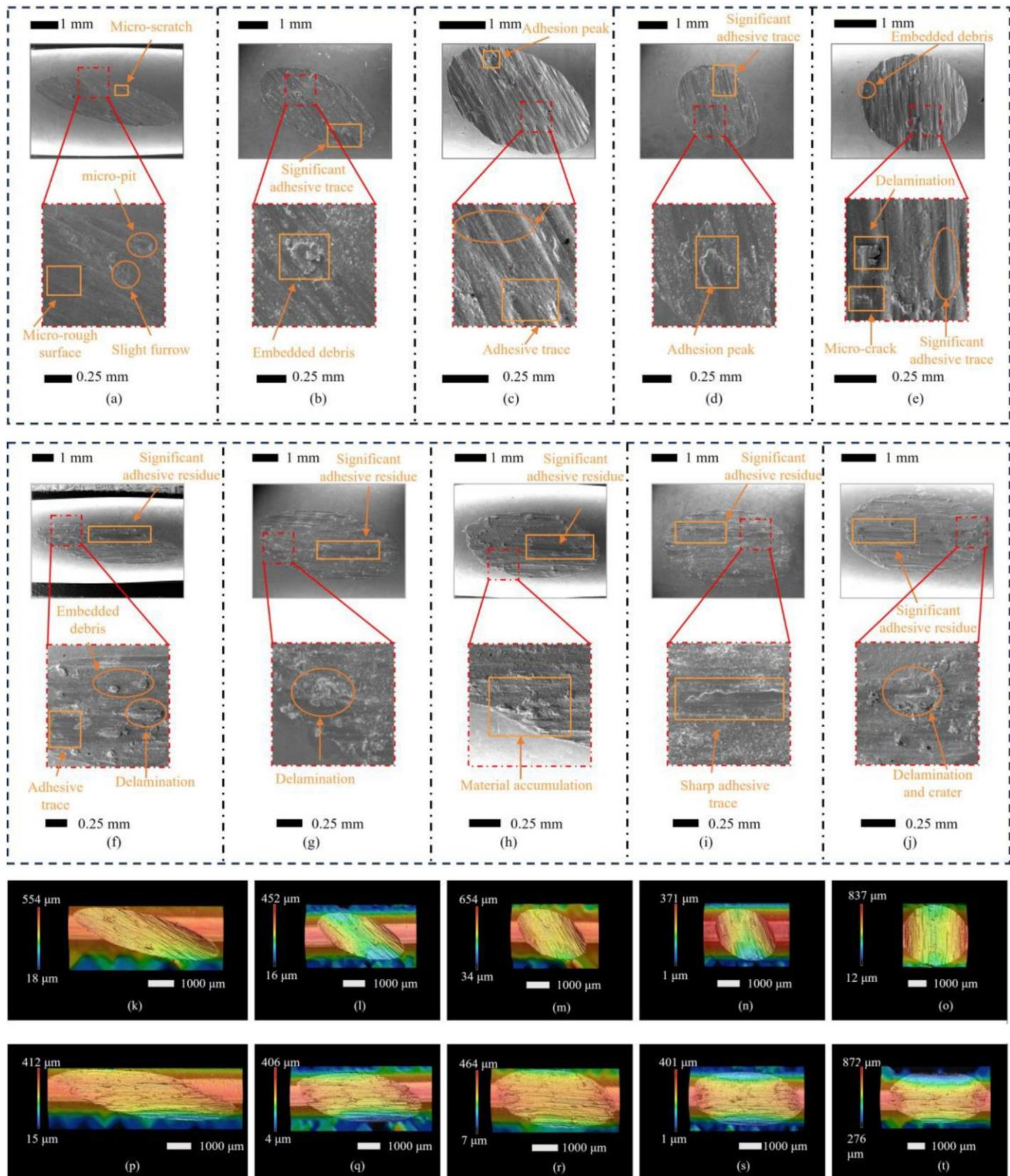
Figure 3. The worn surfaces produced at 30°, 45°, 60°, 75° and 90°, respectively: (a-e) scanning electron microscope (SEM) images of upper surfaces; (f-j) SEM images of lower surfaces; (k-o) laser scanning confocal microscope (LSCM) images of upper surfaces; (p-t) LSCM images of lower surfaces.

Accordingly, adhesive wear and abrasive wear are the primary wear modes. Furthermore, the complexity of the worn surface is nonlinearly related to the friction angle. This may be attributed to the variation in the wear angle affecting the contact area, leading to different wear stages at the same number of friction cycles under different friction angles. In summary, when the friction angle is 30°, the surface wear is relatively mild; however, when the friction angle exceeds 45°, the surface wear situation becomes more complex.

Table 2. The morphologies of worn surfaces at different friction angles.

Surface parameter	Upper surface					Lower surface				
	30	45	60	75	90	30	45	60	75	90
Sa (mm)	40.94	47.69	50.09	54.970	52.23	42.16	50.100	52.16	57.990	60.47
Sz (mm)	397.34	388.75	411.24	407.080	430.11	396.22	422.940	438.73	451.310	448.05
Sq (mm)	52.85	61.12	63.20	69.760	66.44	54.79	64.760	66.97	73.900	78.31
Ssk	0.22	0.29	0.48	0.255	0.55	−0.66	−0.790	−0.68	−0.813	−0.90
Sku	3.02	2.94	2.98	2.800	3.06	3.38	3.521	3.28	3.400	3.61
Sk (mm)	98.70	109.54	110.87	129.930	112.63	93.73	108.480	108.89	115.830	122.70
Spk (mm)	68.73	86.80	93.98	93.930	105.29	43.78	48.240	50.67	52.231	52.67
Svk (mm)	57.01	64.22	56.31	71.400	56.05	90.49	110.940	113.49	130.870	145.46
$Smr1$ (%)	18.20	21.60	21.67	21.000	23.34	12.64	12.320	12.65	11.160	11.67
$Smr2$ (%)	85.57	87.23	87.52	87.130	88.16	78.49	77.590	76.47	74.830	76.64

Figure 3k–t shows the LSCM images of the upper and the lower surfaces obtained from different friction angles. It can be seen that the nadir corresponds to a height of 0. The evolution process of the worn surface morphology with varying friction angles can be observed. Table 2 shows the surface morphology parameters at five different angles. It can be seen that the roughness (Sa) of the worn surface below increases from 42.16 mm to 60.47 mm with the friction angle increasing from $30^{\natural}$ to $90^{\natural}$. The roughness of the upper worn surface also increases, however at a friction angle of $75^{\natural}$, the upper surface roughness is the highest (54.97 ㎚) and not significantly different from the rough- ness of the surface at $90^{\natural}$ (52.23 ㎚). Overall, as the angle increases, the worn surface becomes rougher, but at larger angles, this difference tends to decrease, confirming the trends discussed in the Friction Coefficient and Wear Rate section regarding the changes in friction coefficient and wear rate.

Figure 3k–t shows the LSCM images of the upper and the lower surfaces obtained from different friction angles. It can be seen that the nadir corresponds to a height of 0. The evolution process of the worn surface morphology with varying friction angles can be observed. Table 2 shows the surface morphology parameters at five different angles. It can be seen that the roughness (Sa) of the worn surface below increases from 42.16 ㎚ to 60.47 ㎚ with the friction angle increasing from $30^{\natural}$ to $90^{\natural}$. The roughness of the upper worn surface also increases, however at a friction angle of $75^{\natural}$, the upper surface roughness is the highest (54.97 ㎚) and not significantly different from the rough- ness of the surface at $90^{\natural}$ (52.23 ㎚). Overall, as the angle increases, the worn surface becomes rougher, but at larger angles, this difference tends to decrease, confirming the trends discussed in Friction Coefficient and Wear Rate sec- tion regarding the changes in friction coefficient and wear rate.

The upper worn surface exhibits a considerable number of deep concavities ($Ssk > 0$), while the lower worn surface manifests a significant number of peaks ($Ssk < 0$). With the increase in friction angle, the average height of peaks on the upper surface also increases (Spk increases, $Smr1$ increases), while the average depth of pits on the lower surface also increases (Svk increases, $Smr2$ decreases). This leads to the generation of higher peaks and deeper concavities on both upper and lower surfaces, demonstrating a complementary trend. Surface kurtosis analysis reveals that the kurtosis of the upper surface approaches a normal distribution (Sku approaches 3), indicating a relatively smooth morphology without particularly sharp features. In contrast, the kurtosis values for the lower surface are all greater than 3.28, sug- gesting a sharper morphology on the lower surface.

In summary, the changes in surface morphology are fur- ther intensified with the increase in friction angle, leading to more peaks and concavities and making the worn surface more intricate. This evolution trend is akin to the changes observed in wear rate, especially becoming more pro- nounced at lower angles. Particularly, the worn surface exhibits relatively smooth features at the friction angle of $30^{\natural}$, indicating a comparatively mild level of wear degree.

Tribological behavior analysis under different numbers of friction cycles

Friction coefficient and wear rate
The COF curve over a duration of 28,800 friction cycles within experiment Group 5 (see Table 1) is shown in Fig. 4a. It can be seen that the COF trajectory gradually rises with the increase of friction cycles. Accordingly, the average COF value commences at 0.57919 and increases to 0.66355 when the friction cycles reach to 28,800, indicating severe wear rate. It also can be seen that the COF curve trends to stabilize between 2,400 and 28,800 friction cycles, the aver- age COF value is in the range of [0.62081, 0.66355], and the maximum COF value is in the range of [0.77385, 0.80926]. Afterward, the COF undergoes a steady growth rate. During this wear stage, wear surface analysis is necessary for further analysis of wear modes and wear mechanisms.

Figure 4b–d illustrates the variations in wear amount, wear cross-sectional area, and wear rate according to Fig. 4a. As depicted in Fig. 4b, the wear amount exhibits an almost constant growth rate, with the wear amount for the upper and lower surfaces increasing from 0.35 mg and 0.32 mg at 2,400 friction cycles to 7.77 mg and 5.83 mg at 28,800 fric- tion cycles, respectively. The wear on the upper surface is notably significant, and the difference in wear amount between the upper and lower surfaces gradually widens with increasing friction cycles.

From Fig. 4c, it is observed that the wear cross-sectional area expands with the increasing number of friction cycles, although the growth rate slows down after 14,400 friction cycles. The relationship between wear rate and friction cycles in Fig. 4d follows a similar trend, suggesting that
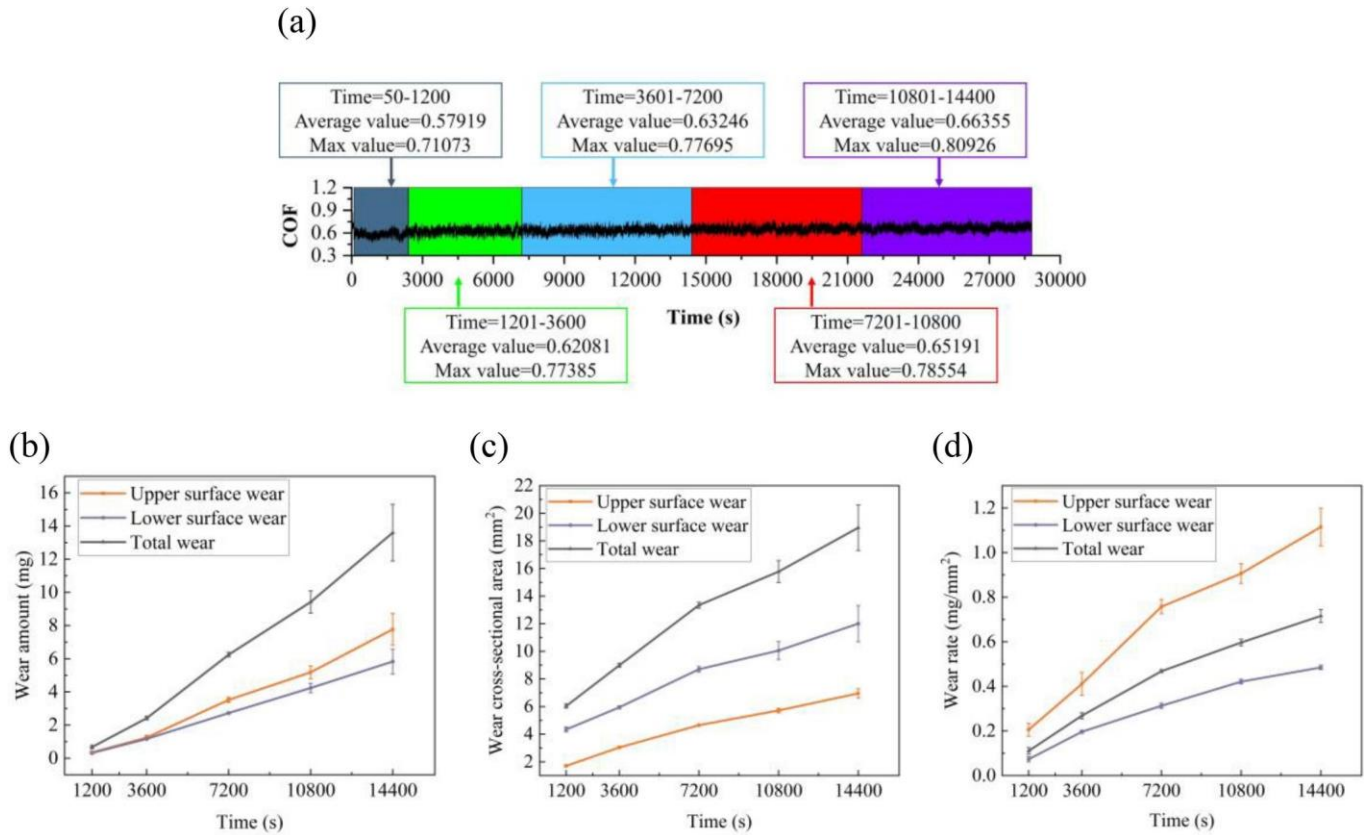
Figure 4. The trend of surface wear over a duration of 28,800 friction cycles within experiment Group 5: (a) coefficient of friction (COF) curve; (b) wear amount; (c) wear cross-sectional area; (d) wear rate.

reaching 14,400 friction cycles might signify the transition from an intense wear phase to a stable one. It is noted that the trend of wear rate is different to that in Archard's curve. This is because the variation of wear area between cylindrical friction pairs and the wear rate is expressed by wear volume per unit area as previously mentioned.

Wear surface

Figure 5 shows the SEM ang LSCM images of the worn surfaces obtained from different cycles. A breaking-in wear phase is observed within 2,400 friction cycles. The worn surfaces display extensive traces of wear debris scraping and delamination structure. After undergoing 7,200 friction cycles, the worn surfaces are accumulated abrasive debris, forming a delamination structure. Meanwhile, regular ware regions are produced. Subsequent to 14,400 friction cycles, the wear degree becomes more severe and the surface morphology becomes more complexity. Locating at the deep wear region, stripping of materials can be seen which is the index of severe wear and indicates that adhesive wear and abrasive wear are occurred. After 21,600 friction cycles, the worn surface resumes smooth, indicating the entry into a new steady wear stage, which is referred to as post-stable wear stage. In contrast, the surface morphology obtained from 28,800 friction cycles re-appears with adhesive wear patterns. This indicates that wear process reenters a more intense stage after a stable wear period due to continued

frictional actions. The evolution of wear states demonstrates a cyclical variation.

The worn surfaces in three-dimensions are shown in Fig. 5k–t. The upper and lower worn surfaces gradually transition from irregular circular and elliptical shapes to regular forms with the increase of friction cycles. The corresponding morphology parameters are listed in Table 3. It can be seen that the Sa, Sz, and Sq values show an upward trend with the increase of friction cycles but the increase rate diminishes.

During 0 to 7,200 friction cycles, the upper surface registers escalating roughness parameters, as denoted by Sa, Sz, and Sq, culminating at values of 34.93 lm, 402.15 lm, and 45.21 lm, respectively. The upper surface shows regular morphology with no sharp peaks, emphasized by the proximity of the Sku to 3.00. In contrast, the lower surface presents more pronounced peaks (Sku exceeding 3, $Ssk < 0$). The valleys of the upper surface (manifesting $Ssk > 0$ and $Smr1 > 1 - Smr2$) and the peaks of the lower surface (characterized by $Ssk < 0$ and $Smr1 < 1 - Smr2$) demonstrate a reciprocal relationship, indicative of a harmonized progression into the phase of steady wear.

During the phase (from 7,200 to 14,400 friction cycles), the visual representation in Fig. 5k–t depicts the adherence of wear debris to the upper surface, thereby engendering more pronounced scratches compared to the initial stage. This augmentation is evidenced by a discernible escalation in both Ssk and Sku, indicating deeper and more substantial
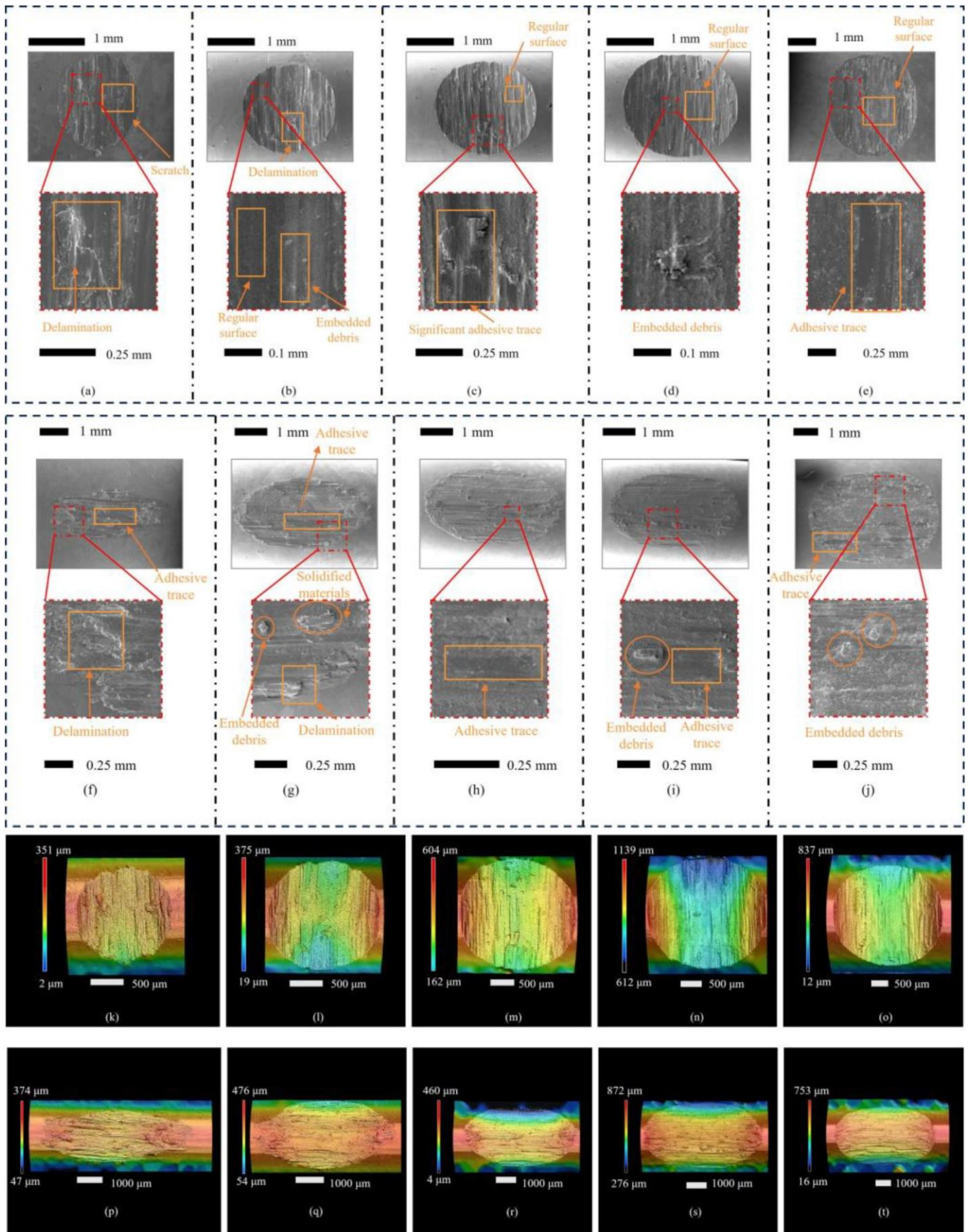
Figure 5. The worn surfaces obtained from 2400, 7200, 14,400, 21,600 and 28,800 friction cycles, respectively: (a-e) scanning electron microscope (SEM) images of upper surfaces; (f-j) SEM images of lower surfaces; (k-o) laser scanning confocal microscope (LSCM) images of upper surfaces; (p-t) LSCM images of lower surfaces.

Table 3. The morphologies of worn surfaces obtained from different friction cycles.

Surface parameter	Upper surface					Lower surface				
	2400	7200	14,400	21,600	28,800	2400	7200	14,400	21,600	28,800
Sa (1m)	25.05	34.93	52.23	64.87	78.92	21.71	38.21	60.47	69.67	81.22
Sz (1m)	287.09	402.15	448.05	488.59	488.96	291.41	340.13	430.11	473.91	542.81
Sq (1m)	31.83	45.21	66.44	82.29	98.94	27.33	49.53	78.31	89.26	100.93
Ssk	−0.30	0.31	0.55	0.58	0.41	−0.21	−0.59	−0.90	−0.73	−0.58
Sku	2.90	2.99	3.06	3.04	2.81	2.89	3.26	3.61	3.27	2.85
Sk (1m)	70.25	81.66	112.63	137.33	178.58	63.78	98.36	122.70	149.84	184.62
Spk (1m)	25.83	63.14	105.29	133.23	147.03	20.56	34.02	52.67	63.82	72.36
Svk (1m)	39.82	46.29	56.05	69.35	87.30	32.05	77.04	145.46	152.52	158.16
$Smr1$ (%)	11.27	19.73	23.34	24.08	22.88	14.06	13.63	11.67	12.15	10.10
$Smr2$ (%)	83.89	85.89	88.16	88.23	89.06	88.38	83.18	76.64	77.10	76.79

grooves. Additionally, the surface undergoes a marked intensification in its degree of roughness, characterized by a heightened value of Sku exceeding 3.00. A noteworthy development is the conspicuous elevation in Spk, which registers at 105.29 1m for the upper surface and 52.67 1m for the lower surface. This phenomenon serves to temper the emergence of additional peaks on the surface. Consequently, this shift manifests a heightened seriousness of wear status, as the wear dynamics transition into a more critical phase.

In the subsequent stage encompassing 14,400 to 21,600 friction cycles, the values of Sku for both the upper and lower surfaces experience reductions to 3.04 and 3.27, respectively. This decline can be attributed to the gradual attenuation of the peaks and valleys, indicative of a smoothing process. This transition signifies the onset of adhesive wear during this specific wear interval, leading to a phenomenon where surface peaks and troughs are rendered less pronounced through a polishing effect.

During the phase from 21,600 to 28,800 friction cycles, the surface gradually becomes smoother (Ssk approaches 0, Sku decreases), and the proportion of peaks and valleys on the worn surface decreases ($Smr1$ decreases, $Smr2$ increases). The wear depth and roughness increase with the number of friction cycles. However, the surface morphology shows an alternating trend of rough-smooth-rough during prolonged wear progress. In summary, the frictional pairs of NiTi alloy mainly undergo four wear stages of breaking-in wear, steady wear, severe wear, and post-stable wear. The surface morphologies fluctuate during the prolong wear process to show different wear mechanisms, including abrasive wear, adhesive wear, and fatigue wear.

Tribological behavior analysis under different lubrications

Friction coefficient

Within in vitro experiments, the replication of actual lubrication conditions within blood vessels remains unattainable. Consequently, investigations are executed under varied lubrication settings to gauge the performance of the NiTi alloy. Figure 6 is the COF curves corresponding to distinct lubrication conditions, encompassing 25% calf serum, PBS solution and dry friction.

This visual representation substantiates a notable observation: the COF when subject to 25% calf serum is significantly lower in contrast to both dry friction and PBS solution. Furthermore, the COF curve exhibits under 25% calf serum conditions exhibits marked fluctuations. This behavior is attributed to the detachment of sizable wear debris from the worn surface due to fatigue wear, as discerned from Fig. 6. Despite this phenomenon, the worn surface undergoes a rapid process of wear pit refilling and subsequent smoothing within a brief span of time.

The wear amount, wear cross-sectional area, and wear rate sustained by the friction pairs within varying lubrication conditions are presented in Table 4. Notably, the recorded wear for both the upper and lower friction pairs in the context of 25% calf serum are exceptionally minute, with the value of wear amount falling below 0.01 mg, the value of wear cross-sectional area falling below 2.75 mm², and the value of wear rate falling below 0.06 mg/mm². Under the PBS lubricating conditions, there is a significant difference in the wear rates between the upper and the lower surfaces. This lubrication condition results in a reduction of wear rate on the lower surface, while simultaneously increasing wear rate on the upper surface. The minimum wear amount and wear rate under the calf serum lubricating condition may be contributed by the proteins and organic substances included in the calf serum, which can form lubricating film on the friction surface to reduce wear rate.

Wear surface

Figure 7 respectively show the SEM and LSCM images of worn surfaces subjected to diverse lubrication conditions. It is observed that the surface topography engendered by calf serum lubrication is considerably less pronounced in comparison to the outcomes witnessed under dry friction and PBS lubrication settings. The meticulously extracted surface morphologies from these worn surfaces are comprehensively documented in Table 5.

The morphologies of the worn surfaces under dry friction and PBS lubrication conditions are similar, but with significant differences under calf serum lubrication, as shown in Fig. 7a–f. Smooth surface with regular penetrating scratches appears under the calf serum lubrication. In contrast, the worn surfaces produced under PBS lubrication and dry friction conditions exhibit regular short scratches. Wide adhesive surfaces and adhesive peaks are also caused by adhesive wear, leading to a stratified surface structure. It also can be seen micro-pits on the lower worn surface. Moreover, materials are easier to fall off from the friction pairs under dry
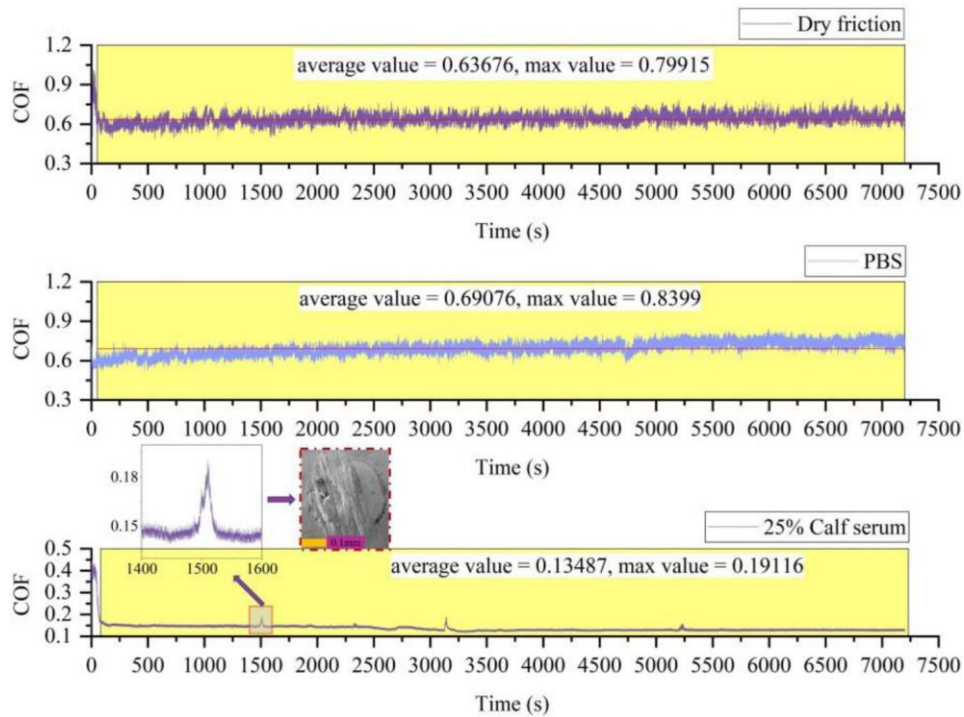
Figure 6. The coefficient of friction (COF) curves obtained from different lubrication conditions.

Table 4. The wear amount of friction pairs in different lubrication conditions.

Wear loss parameter	25% calf serum	PBS	Dry friction
Wear amount of upper surface (mg)	<0.01	6.83	3.52
Wear cross-sectional area of upper surface (mm²)	0.47	6.13	4.65
Wear rate of upper surface (mg/mm²)	<0.21	1.11	0.76
Wear amount of lower surface (mg)	<0.01	2.69	2.72
Wear cross-sectional area of lower surface (mm²)	2.75	10.40	8.70
Wear rate of lower surface (mg/mm²)	<0.04	0.26	0.31
Total wear amount (mg)	<0.02	9.52	6.24
Total wear cross-sectional area (mm²)	3.22	16.53	13.35
Total wear rate (mg/mm²)	<0.06	0.57	0.47

friction condition, and the flushing action of the lubricants may contribute to the material stripping.

Remarkably, under calf serum lubrication, both the upper surface (characterized by Sa measuring 14.73 1m, Sz measuring 117.72 1m, and Sq at 17.90 1m) and the lower surface (with Sa at 17.14 1m, Sz at 251.48 1m, and Sq at 21.39 1m) present the subtlest contour deviations when compared to other lubrications.

Furthermore, the upper surface encountering calf serum lubrication demonstrates a Sku value lower than 3.00, indicating a reduced prevalence of surface peaks. Conversely, higher $Smr1$ and $Smr2$ values corresponding to dry friction and PBS lubrication signify a greater propensity for the generation of both peaks and valleys on the worn surface.

Discussion

In order to comprehensively evaluate the influence of friction angles on the tribological characteristics of NiTi alloy woven vascular stents, a series of simulated experiments were conducted using an *in vitro* friction tester. This analysis, including parameters such as friction coefficient, wear loss, and surface morphology, provides an in-depth understanding of the impact of friction angles on the wear of NiTi alloy woven vascular stents. The experimental results show that the mildest wear is produced in the friction angle of 30° than other friction angles. The wear becomes more serious with the increase of friction angles. These results may be caused by the following three factors:

1. Smaller friction angle may lead to a larger line-to-line contact area for the friction pairs, and friction forces are dispersed in a larger support area. Inversely, larger friction angle may increase the contact stress on per unit area, which can be seen in Fig. 3.
2. Smaller friction angles may contribute to a more uniform distribution of frictional heat, reducing the likelihood of localized high temperatures that could induce wear. This contributes to maintaining the stability of the stent surface.
3. More wear debris is produced from larger friction angle than that of smaller friction angle. Owing to the wear debris may cause severe abrasive wear, which can accelerate wear rate, much more serious wear is occurred under larger friction angles. Accordingly, smaller friction angle exhibits milder wear degree.
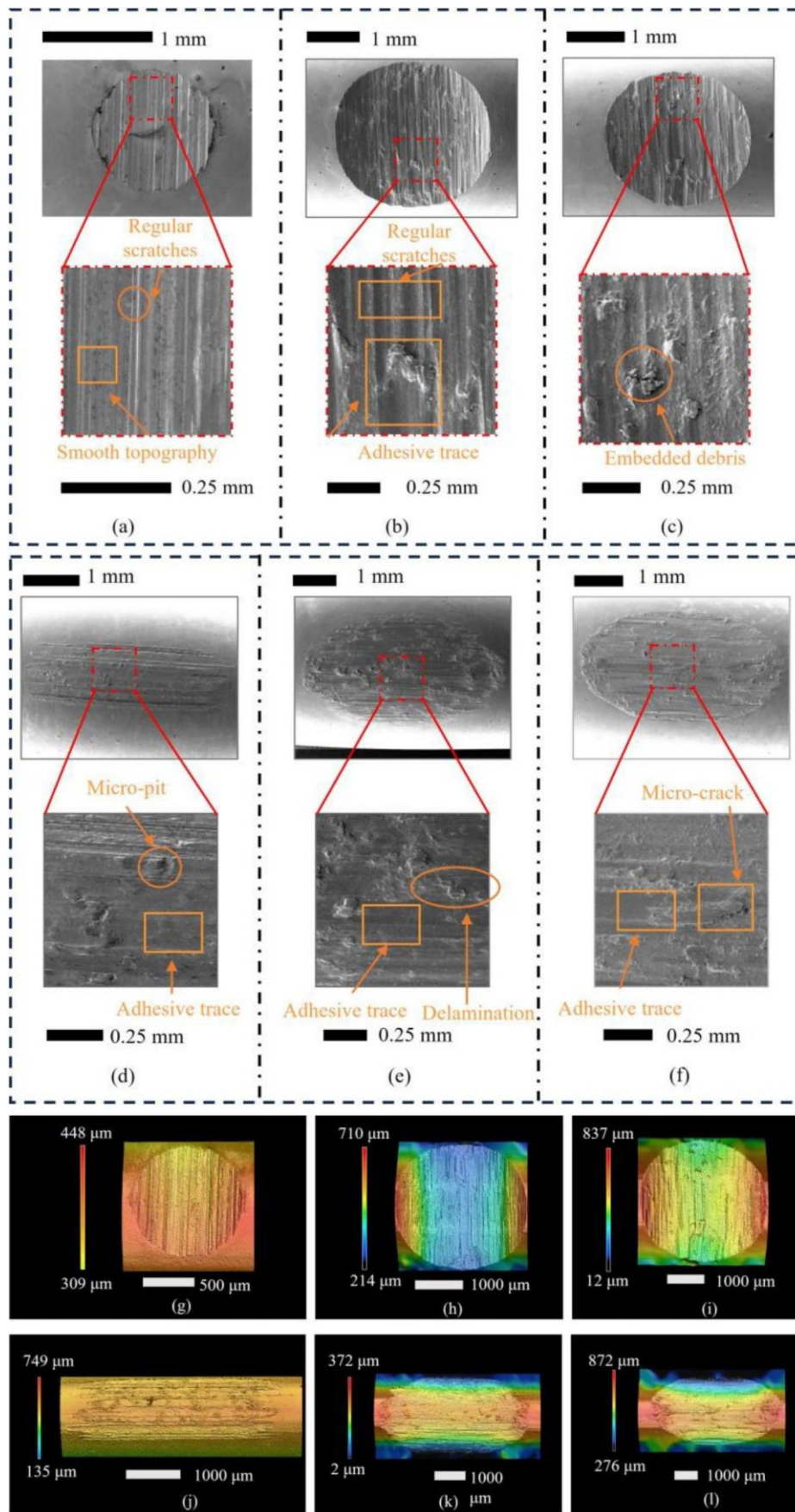
Figure 7. The worn surfaces obtained from 25% calf serum, PBS, and dry friction, respectively: (a–c) scanning electron microscope (SEM) images of upper surfaces; (d–f) SEM images of lower surfaces; (g–i) laser scanning confocal microscope (LSCM) images of upper surfaces; (j–l) LSCM images of lower surfaces.

Table 5. The morphologies of the worn surfaces in different lubrication conditions.

Surface parameter	Upper surface			Lower surface		
	25% calf serum	PBS	Dry friction	25% calf serum	PBS	Dry friction
Sa (1m)	14.73	69.21	52.23	17.14	71.36	60.47
Sz (1m)	117.72	469.70	430.11	251.48	507.68	448.05
Sq (1m)	17.90	87.35	66.44	21.39	90.81	78.31
Ssk	0.23	1.08	0.55	−0.76	−1.10	−0.90
Sku	2.78	3.29	3.16	3.42	3.96	3.68
Sk (1m)	39.68	126.50	112.63	41.41	125.35	122.70
Spk (1m)	20.95	175.81	105.29	9.61	44.97	52.67
Svk (1m)	10.73	38.39	56.05	33.97	181.12	145.46
Smr1 (%)	14.99	27.19	23.34	6.49	8.45	11.67
Smr2 (%)	91.12	92.82	88.16	78.37	72.23	76.64

While this study systematically analyzed the impact of friction angles on wear, limitations arise due to the small dimensions of vascular stents and the stringent conditions of the in vivo environment. The research fell short of fully simulating experiments with practical applications. Discrepancies exist in material dimensions, loads, and lubrication environments compared to the *in vivo* conditions. Although the results and analysis clearly indicate that smaller friction angles lead to less wear, the extent of the differences in wear states caused by variations in friction angles in a real *in vivo* environment remains unclear. Therefore, further research is warranted to delve deeper into the degree to which the design of small friction angles contributes to improving the wear resistance of vascular stents.

Additionally, the wear behaviors of NiTi alloy vary under different lubrication conditions. While PBS can simulate the osmotic pressure of the human body, its wear situation significantly differs from that of bovine serum. There is a notable distinction between PBS buffer solution and the real blood environment inside the human body. Despite that the anticoagulants are helpful for assessing the biocompatibility of materials and reducing the risk of thrombus formation. The anticoagulants are not suggested using in friction and wear experiments. This is because the friction and wear experiments are to evaluate the tribological performance between friction pairs and explore the physical properties between materials rather than biological processes within the liquid phase. Therefore, in conducting external wear-related experiments on vascular stents, it is necessary to explore a new lubricating medium that more closely mimics the blood environment in the body to ensure the meaningfulness of the research results.

Conclusion

To comprehensively evaluate NiTi alloy woven vascular stents regarding friction angles, simulated *in vitro* experiments were conducted. Parameters such as friction coefficient, wear loss, and surface morphology were analyzed to understand the impact of friction angles on NiTi alloy braided vascular stents. Key findings include:

1. The friction angle significantly influences vascular scaffold interface wear. At $30^{\natural}$, wear loss is minimized, exhibiting the lowest average friction coefficients, wear rates, surface roughness, and maximum wear depth. In comparison to $90^{\natural}$, the wear rate decreases by 32%, and surface roughness is reduced by 22%. Higher friction angles (larger than $60^{\natural}$) exhibit similar wear conditions, underscoring the importance of adopting lower friction angles to enhance wear resistance.

2. The wear progression of NiTi friction pairs exhibits distinct phases: breaking-in wear, steady wear, severe wear, and post-stable wear, the wear stages demonstrate alternating trends with the increase of friction cycles, obtaining the long-term wear behavior inherent to NiTi friction pairs with adhesive wear and abrasive wear mechanisms.

3. Comparative analysis of dry friction, PBS, and 25% calf serum lubricated friction regimes indicates the suitability of NiTi in bodily lubrication environments. The resemblance between calf serum and blood lubrication characteristics highlights the compatibility of reinforced NiTi in vascular stent applications. Future research should involve clinical testing to validate NiTi stents' performance in real-world settings.

Disclosure statement

No potential conflict of interest was reported by the author(s).

Funding

References

(1) Wang, Y., Chen, L., Hou, R., Bai, L., and Guan, S. (2023), "Rapamycin-Loaded Nanocoating to Specially Modulate Smooth Muscle Cells on ZE21B Alloy for Vascular Stent Application," *Applied Surface Science*, **615**, pp 156410. doi:10.1016/j.apsusc.2023.156410

(2) Jaziri, H., Mokhtar, S., Chakfe, N., Heim, F., and Abdessalem, S. B. (2019), "Elastic Recovery of Polymeric Braided Stents under Cyclic Loading: Preliminary Assessment," *Journal of the Mechanical Behavior of Biomedical Materials*, **98**, pp 131–136. doi:10.1016/j.jmbbm.2019.06.018

(3) Jaziri, H., Mokhtar, S., Kyosev, Y., Chakfe, N., Heim, F., and Ben Abdessalem, S. (2022), "Influence of Fatigue Stress on the Radial Strength of Polymeric Braided Vascular Stents," *Polymers*

for Advanced Technologies, **33**, pp 627–637. doi:10.1002/pat. 5544

(4) Zhang, X., Zhang, Y., and Jin, Z. (2022), "A Review of the Bio-Tribology of Medical Devices," *Friction*, **10**, pp 4–30. doi:10. 1007/s40544-021-0512-6

(5) Pan, C., Han, Y., and Lu, J. (2021), "Structural Design of Vascular Stents: A Review," *Micromachines*, **12**, pp 770. doi:10. 3390/mi12070770

(6) Clark, E. R., Porter, K. E., and Bryant, M. G. (2019), "Fretting-Corrosion of Cardiovascular Stent Materials: The Role of Electrochemical Polarisation on Debris Generation Mechanisms," *Biotribology*, **18**, pp 100093. doi:10.1016/j.biotri. 2019.100093

(7) Im, S. H., Jung, Y., and Kim, S. H. (2017), "Current Status and Future Direction of Biodegradable Metallic and Polymeric Vascular Scaffolds for Next-Generation Stents," *Acta Biomaterialia*, **60**, pp 3–22. doi:10.1016/j.actbio.2017.07.019

(8) Levintant-Zayonts, N., Starzynski, G., and Kucharski, S. (2021), "On the Origin of Superiority in Wear Response of Superelastic NiTi Compared to Conventional Ti6Al4V," *Tribology Transactions*, **64**, pp 287–301. doi:10.1080/10402004.2020. 1836295

(9) Kapnisis, K. K., Halwani, D. O., Brott, B. C., Anderson, P. G., Lemons, J. E., and Anayiotos, A. S. (2013), "Stent Overlapping and Geometric Curvature Influence the Structural Integrity and Surface Characteristics of Coronary Nitinol Stents," *Journal of the Mechanical Behavior of Biomedical Materials*, **20**, pp 227–236. doi:10.1016/j.jmbbm.2012.11.006

(10) Prithipaul, P. K. M., Kokkolaras, M., and Pasini, D. (2018), "Assessment of Structural and Hemodynamic Performance of Vascular Stents Modelled as Periodic Lattices," *Medical Engineering & Physics*, **57**, pp 11–18. doi:10.1016/j.medengphy. 2018.04.017

(11) Sanmartın, M., Goicolea, J., Garcıa, C., Garcıa, J., Crespo, A., Rodrıguez, J., and Goicolea, J. M. (2006), "Influence of Shear Stress on In-Stent Restenosis: In Vivo Study Using 3D Reconstruction and Computational Fluid Dynamics," *Revista Espan~ola de Cardiologıa (English Edition)*, **59**, pp 20–27. doi:10. 1016/S1885-5857(06)60044-3

(12) Wang, Y., Wu, H., Fan, S., Wu, J., and Yang, S. (2023), "Structure Design and Mechanical Performance Analysis of Three Kinds of Bioresorbable Poly-Lactic Acid (PLA) Stents," *Computer Methods in Biomechanics and Biomedical Engineering*, **26**, pp 25–37. doi:10.1080/10255842.2022.2045485

(13) Liu, R., Xu, S., Luo, X., and Liu, Z. (2020), "Theoretical and Numerical Analysis of Mechanical Behaviors of a Metamaterial-Based Shape Memory Polymer Stent," *Polymers*, **12**, pp 1784. doi:10.3390/polym12081784

(14) Weaver, J. D., Ramirez, L., Sivan, S., and Di Prima, M. (2018), "Characterizing Fretting Damage in Different Test Media for Cardiovascular Device Durability Testing," *Journal of the Mechanical Behavior of Biomedical Materials*, **82**, pp 338–344. doi:10.1016/j.jmbbm.2018.04.004

(15) Kim, Y.-S., and Kim, J.-G. (2019), "Electrochemical Corrosion Behavior of a Non-Vascular, Bi-Stent Combination, Surgical Esophageal Nitinol Stent in Phosphate-Buffered Saline Solution," *Materials Science & Engineering. C, Materials for Biological Applications*, **94**, pp 821–830. doi:10.1016/j.msec.2018. 10.017

(16) Jiang, J., Huang, H., Niu, J., Zhu, D., and Yuan, G. (2022), "Fabrication and Characterization of Biodegradable Zn-Cu-Mn Alloy Micro-Tubes and Vascular Stents: Microstructure, Texture, Mechanical Properties and Corrosion Behavior," *Acta Biomaterialia*, **151**, pp 647–660. doi:10.1016/j.actbio.2022.07.049

(17) Surovtseva, M. A., Poveschenko, O. V., Kuzmin, O. S., Kim, I. I., Kozhukhov, A. S., BondareNKo, N. A., Chepeleva, E. V., Kolodin, A. N., Lykov, A. P., Shcheglov, D. V., Pichugin, V. F., and Yu. Zhuravleva, I. (2022), "Titanium Oxide– and Oxynitride–Coated Nitinol: Effects of Surface Structure and Composition on Interactions with Endothelial Cells," *Applied*

(18) Lopes, N. I. A., Henrique Jardim Freire, N., Resende, P. D., Santos, L. A., and Buono, V. T. L. (2018), "Electrochemical Deposition and Characterization of ZrO2 Ceramic Nanocoatings on Superelastic NiTi Alloy," *Applied Surface Science*, **450**, pp 21–30. doi:10.1016/j.apsusc.2018.04.154

(19) Chu, B., Li, X., Fan, S., He, J., Ge, X., Li, H., Chen, C., Wang, Z., Wang, S., and Li, B. (2023), "CD34 Antibody-Coated Biodegradable Fiber Membrane Effectively Corrects Atrial Septal Defect (ASD) by Promoting Endothelialization," *Polymers*, **15**, pp 108. doi:10.3390/polym15010108

(20) Cameron, N., and Farhat, Z. (2019), "Fabrication, Characterization, and Evaluation of Monolithic NiTi Nanolaminate Coatings," *Tribology Transactions*, **62**, pp 1007–1018. doi:10.1080/10402004.2019.1640331

(21) Li, Z., Farhat, Z., Jarjoura, G., Fayyad, E., Abdullah, A., and Hassan, M. (2019), "Synthesis and Characterization of Scratch-Resistant Ni-P-Ti-Based Composite Coating," *Tribology Transactions*, **62**, pp 880–896. doi:10.1080/10402004.2019. 1634227

(22) Trepanier, C., Gong, X.-Y., Ditter, T., Pelton, A., Neely, Y., Grishaber, R. (2006), "Effect of Wear and Crevice on the Corrosion Resistance of Overlapped Stents," *SMST-2006 - Proceedings of the International Conference on Shape Memory and Superelastic Technologies*. doi:10.1361/cp2006smst265

(23) Podgornik, B., Hogmark, S., and Pezdirnik, J. (2004), "Comparison between Different Test Methods for Evaluation of Galling Properties of Surface Engineered Tool Surfaces," *Wear*, **257**, pp 843–851. doi:10.1016/j.wear.2004.05.005

(24) Berger, M., and Hogmark, S. (2002), "Tribological Properties of Selected PVD Coatings When Slid against Ductile Materials," *Wear*, **252**, pp 557–565. doi:10.1016/S0043-1648(02)00011-X

(25) Wang, S., Zhang, Y., Qin, Y., Lu, J., and Liu, W. (2023), "Improvement of TiN Coating on Comprehensive Performance of NiTi Alloy Braided Vascular Stent," *Ceramics International*, **49**, pp 13405–13413. doi:10.1016/j.ceramint.2022.12.215

(26) Rodrigues, A., Figueiredo, L., and Bordado, J. (2013), "Abrasion Behaviour of Polymeric Textiles for Endovascular Stent-Grafts," *Tribology International*, **63**, pp 265–274. doi:10.1016/j.triboint. 2012.11.003

(27) Ho, K.-L., Hung, M.-Y., Chen, J.-H., Jian, Y.-M., and Hsiao, H.-M. (2019), "Design and Testing of a New Vascular Stent with Enhanced Fatigue Life," *IOP Conference Series: Materials Science and Engineering*, **644**, pp 012015. doi:10.1088/1757-899X/644/1/012015

(28) Peng, Y., Yue, H., Wang, S., Cao, G., Wu, H., and Liu, C. (2023), "Probability-Weighted Ensemble Support Vector Machine for Intelligent Recognition of Moving Wear Debris from Joint Implant," *Tribology International*, **186**, pp 108583. doi:10.1016/j.triboint.2023.108583

(29) Wichelhaus, A., Eichenberg, T., Gruber, P., Bamidis, E. P., and Stocker, T. (2022), "Friction Force Adjustment by an Innovative Covering System Applied with Superelastic NiTi Brackets and Wires—An in-Vitro Study," *Materials*, **15**, pp 4248. doi:10. 3390/ma15124248

(30) Li, Y., Zhang, F., Zhao, T.-T., Tang, M., and Liu, Y. (2014), "Enhanced Wear Resistance of NiTi Alloy by Surface Modification with Nb Ion Implantation," *Rare Metals*, **33**, pp 244–248. doi:10.1007/s12598-014-0223-5

(31) Huang, X., Kang, N., Coddet, P., and El Mansori, M. (2023), "Analyses of the Sliding Wear Behavior of NiTi Shape Memory Alloys Fabricated by Laser Powder Bed Fusion Based on Orthogonal Experiments," *Wear*, **534-535**, pp 205130. doi:10. 1016/j.wear.2023.205130

(32) Hongtao, L., Shirong, G., Shoufan, C., and Shibo, W. (2011), "Comparison of Wear Debris Generated from Ultra High Molecular Weight Polyethylene in Vivo and in Artificial Joint Simulator," *Wear*, **271**, pp 647–652. doi:10.1016/j.wear.2010.11. 012

(33) Li, J., Wang, S., Fu, S., and Peng, Y. (2023), "Study on Wear Debris Characteristics of Different Polyethylene under Reciprocating Sliding and Compound Motion Modes," *Wear*, **530-531**, pp 205062. doi:10.1016/j.wear.2023.205062

(34) Yoosefan, F., Ashrafi, A., and Vaghefi, S. M. M. (2023), "Enhanced Mechanical and Corrosion Properties of Cold-Rolled CoCrFeMoNi High-Entropy Alloy, as a Proposed Material for Vascular Stents," *Materials Characterization*, **205**, pp 113343. doi:10.1016/j.matchar.2023.113343

(35) Li, J., Wang, S., Wang, F., Yu, X., and Xu, L. (2023), "Insight on the in Vivo Wear Characteristics of Goat Artificial Cervical Disc Implanted for 6 Months," *Journal of the Mechanical Behavior of Biomedical Materials*, **143**, pp 105909. doi:10.1016/j.jmbbm.2023.105909

(36) Hu, X., Song, J., Liao, Z., Liu, Y., Gao, J., Menze, B., and Liu, W. (2022), "Morphological Residual Convolutional Neural Network (M-RCNN) for Intelligent Recognition of Wear Particles from Artificial Joints," *Friction*, **10**, pp 560–572. doi:10.1007/s40544-021-0516-2

(37) Cui, L., Lu, Y., Gong, C., Li, H., Huang, J., and Xiong, D. (2023), "Metal Ion Reinforced Hydrogel/Ti6Al4V Bionic Composite Joint Bearing Interface with Extraordinary Mechanical and Biotribological Properties," *Tribology International*, **189**, pp 109024. doi:10.1016/j.triboint.2023.109024

(38) Feng, C., Cao, Y., Wu, T., Cen, J., Chen, K., Li, X., and Zhang, D. (2023), "Friction and Wear Mechanism of Artificial Joint Composite Material PEEK/ZnO under Different Decomposition Motion Modes of Knee Joint," *Tribology International*, **189**, pp 108917. doi:10.1016/j.triboint.2023.108917

(39) Peng, Y., Wu, Z., Cao, G., Wang, S., Wu, H., Liu, C., and Peng, Z. (2021), "Three-Dimensional Reconstruction of Wear Particles by Multi-View Contour Fitting and Dense Point-Cloud Interpolation," *Measurement*, **181**, pp 109638. doi:10.1016/j.measurement.2021.109638

(40) Angermann, C., Haltmeier, M., Laubichler, C., Jonsson, S., Schwab, M., Moravova, A., Kiesling, C., Kober, M., and Fimml, W. (2023), "Surface Topography Characterization Using a Simple Optical Device and Artificial Neural Networks," *Engineering Applications of Artificial Intelligence*, **123**, pp 106337. doi:10.1016/j.engappai.2023.106337

(41) Niemczewska-Wojcik, M., Pethuraj, M., Uthayakumar, M., and Abdul Majid, M. S. (2022), "Characteristics of the Surface Topography and Tribological Properties of Reinforced Aluminum Matrix Composite," *Materials*, **15**, pp 358. doi:10.3390/ma15010358